CHEMISTRY OF MATERIALS
pubs.acs.org/cm
Article

A Low-Temperature Growth Mechanism for Chalcogenide Perovskites

Ruiquan Yang, Jessica Nelson, Calvin Fai, Hasan Arif Yetkin, Chase Werner, Merielle Tervil, Alexander D. Jess, Phillip J. Dale, and Charles J. Hages*

Cite This: https://doi.org/10.1021/acs.chemmater.3c00494
Read Online
ACCESS | Metrics & More | Article Recommendations | Supporting Information

ABSTRACT: Chalcogenide perovskites have attracted increasing research attention in recent years due to their promise of unique optoelectronic properties combined with stability. However, the synthesis and processing of these materials has been constrained by the need for high temperatures and/or long reaction times. In this work, we address the open question of a low-temperature growth mechanism for $BaZrS_3$. Ultimately, a liquid-assisted growth mechanism for $BaZrS_3$ using molten BaS_3 as a flux is demonstrated at temperatures ≥540 °C in as little as 5 min. The role of Zr-precursor reactivity and $S_{(g.)}$ on the growth mechanism and the formation of $Ba_3Zr_2S_7$ is discussed, in addition to the purification of resulting products using a straightforward H_2O wash. The extension of this growth mechanism to other Ba-based chalcogenides is shown, including $BaHfS_3$, $BaNbS_3$, and $BaTiS_3$. In addition, an alternative vapor-transport growth mechanism is presented using S_2Cl_2 for the growth of $BaZrS_3$ at temperatures as low as 500 °C in at least 3 h. These results demonstrate the feasibility of scalable processing for the formation of chalcogenide perovskite thin-films.

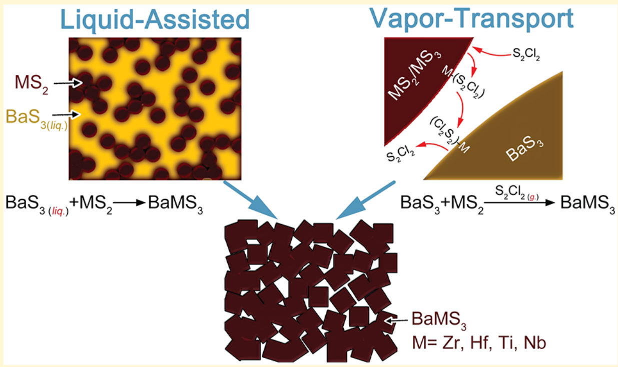

1. INTRODUCTION

Chalcogenide perovskites have gained recent research attention due to their potential as Pb-free, inorganic perovskite semiconductors. Compared to hybrid halide perovskites, such as $CH_3NH_3PbI_3$, these chalcogenide perovskites have significantly improved structural stability.[1−3] Compared to oxide perovskites, the inclusion of S or Se as anions reduces the band gap for applications with visible and NIR light. $BaZrS_3$ in particular has been a primary focus in recent research, possessing promising optoelectronic properties (primarily identified from theory) including band gap values relevant for photovoltaics, an extraordinarily high absorption coefficient, tolerance to deep defects, strong dielectric screening, favorable phonon properties, and desirable (isotropic) electron mobility for efficient charge transport.[3−9] Additionally, $BaZrS_3$ is comprised of nontoxic and earth-abundant constituents.

However, the majority of reported syntheses require high temperatures and/or long reaction times.[4,5] Such reactions have kinetic limitations—for example, due to solid-state growth techniques—and/or thermodynamic limitations—for example, using highly stable oxide precursors. $BaZrS_3$ powders were reported as early as 1957 by Hahn and Mutschke[10] via annealing of binary sulfides (BaS, ZrS_2) at 900 °C for 2 weeks. Alternatively, Clearfield[11] reported the reaction of $BaZrO_3$ with CS_2 at 950−1200 °C in 1963. Similar reactions were reported over the following 60 years using mixtures of BaS, ZrS_2, $BaCO_3$, ZrO_2, and $BaZrO_3$. Recent progress in the synthesis of $BaZrS_3$ thin films is summarized in the following reactions. Márquez et al.[12] and Wei et al.[13] formed $BaZrS_3$ via pulsed laser deposition (PLD) using a Ba−Zr−O target followed by annealing in a reactive sulfur species at ca. 800−1050 °C. Alternatively, Yu et al.[14] used a Ba−Zr−S target in PLD followed by an anneal with CS_2 at 900 °C, and Surendran et al.[15] grew an expitaxial thin film of $BaZrS_3$ from a $BaZrS_3$ target using PLD in an H_2S environment at 700−850 °C. Comparotto et al.[16] formed $BaZrS_3$ via cosputtering of Ba−Zr−S followed by sulfur-annealing from 650−900 °C. Sadeghi et al.[17] reported $BaZrS_3$ grown via molecular beam epitaxy (MBE) at 900 °C. Gupta et al.[18] reported $BaZrS_3$ via sulfurization of $BaZrO_3$ at 1050 °C. While high-quality films were obtained in all these reports, oxidation is commonly reported and many of the methods require specialized equipment. Practical fabrication of $BaZrS_3$ and other chalcogenide perovskites will require more moderate fabrication temperatures and shorter reaction times for cost-effective

Received: March 2, 2023
Revised: May 17, 2023

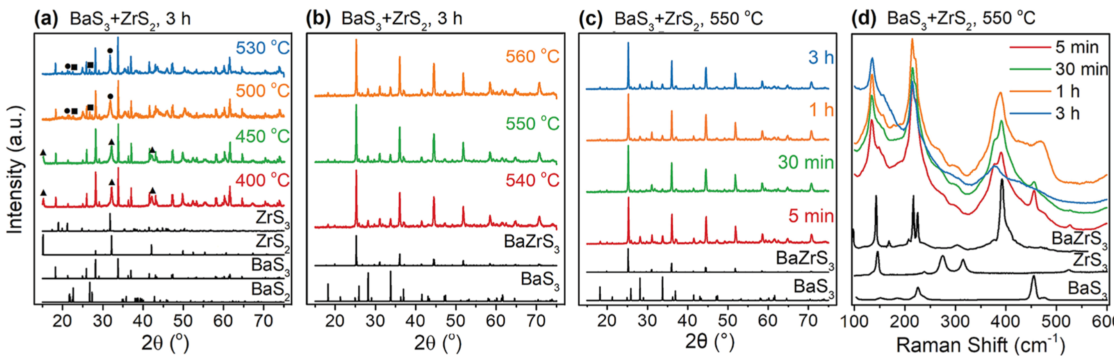

Figure 1. XRD patterns of samples from BaS_3 + ZrS_2 reactions (a) for 3 h at 400 °C, 450 °C, 500 °C, and 530 °C (triangles label ZrS_2, circles label for ZrS_3, and rectangles label BaS_2); (b) for 3 h at 540 °C, 550 °C, and 560 °C; and (c) at 550 °C for 5 min, 30 min, 1 h, and 3 h. (d) Raman spectra of samples from the reaction times in (c). Reference XRD patterns are shown in black labeled by compound (BaS_2 PDF 01-071-0377, BaS_3 PDF 01-073-1177, ZrS_2 PDF 01-089-4822, ZrS_3 PDF 01-080-0926, $BaZrS_3$ PDF 01-073-0847). Reference Raman spectrum for $BaZrS_3$ is from Gross et al. (measured at 14 K),[19] while ZrS_3 and BaS_3 are measured on our synthesized precursors (see SI).

manufacturing and the use of traditional substrates, such as glass.

Preparation of $BaZrS_3$ at lower temperatures has drawn recent attention, though this research is still at an early stage. We recently reported the synthesis of $BaZrS_3$ nanoparticles at 330 °C,[20] with similar results reported by Zilevu at al.[21] Such nanoparticles are yet to be processed into device-grade films. Turnley et al.[22] reported the solution-based synthesis of $BaZrS_3$ via sulfurization of an organometallic Ba precursor and ZrH_2 at temperatures above 550 °C; however, continuous, dense films were not possible in this approach. While these experiments demonstrate the ability for $BaZrS_3$ to form at moderate temperatures, little is known about the low-temperature growth mechanism. For instance, Wang et al.[23] reported a reaction for $BaZrS_3$ powders at 600 °C (7 days) using very specific annealing conditions in a slight excess of sulfur vapor. This interesting reaction mechanism was not thoroughly considered until a recent review by Sopiha et al.[4] where the importance of BaS_3 for the "fast formation" of $BaZrS_3$ was suggested. Thus, Comparotto et al.[24] reported a similarly inspired sulfur-anneal on a cosputtered Ba−Zr film for the formation of $BaZrS_3$ at 590 °C (using a SnS_2 capping layer to prevent oxidation). Wang et al.[23] also reported the synthesis of $BaZrS_3$ (7 days) at temperatures as low as 450 °C if a small amount of BaS is replaced with $BaCl_2$, though the mechanism for this reaction was unknown. Niu et al.[25] also reported the synthesis of $BaZrS_3$ (and $SrZrS_3$) from BaS/SrS, Zr, and S at 600 °C with the inclusion of I_2 (60 h—though it is unclear if the reaction happens faster). We note that during the review stage of this work, Vincent et al.[26] reported a liquid flux-assisted growth mechanism for $BaZrS_3$ and $BaHfS_3$ whose results are complementary to that reported herein.

In this work, we address the open question of a low-temperature growth mechanism for $BaZrS_3$. A systematic study of the reaction conditions (precursor composition, reaction time/temperature, precursor reactivity, and the use of halide catalysts) is reported. Ultimately, we achieve the rapid synthesis of $BaZrS_3$ via annealing of BaS_3 and ZrS_2 in as little as 5 min at 550 °C. A liquid-assisted grain growth mechanism in molten BaS_3 is responsible for the rapid, low-temperature growth. Alternatively, we demonstrate that the reaction temperature can be further reduced to 500 °C (below the melting point of BaS_3) via the addition of a chloride catalyst, albeit at a slower reaction rate. The reactivity of Zr precursors decreases successively from ZrS_2, Zr-(S_2Cl_2), ZrS_3, to Zr-metal. The $Ba_3Zr_2S_7$ phase is obtained with low-reactivity Zr metal, while $BaZrS_3$ forms with the more reactive precursors. The resulting $BaZrS_3$ from liquid-assisted grain growth can be purified from residual BaS_3-flux with a water wash. In contrast, $Ba_3Zr_2S_7$ is found to be unstable in water and converts to the $BaZrS_3$ phase. The formation conditions for unwanted binaries, such as ZrS_3, BaS_2, and BaS, are discussed. Finally, we extend the liquid-assisted growth mechanism to demonstrate similar results for $BaHfS_3$, $BaNbS_3$, and $BaTiS_3$.

2. RESULTS AND DISCUSSION

2.1. Liquid (BaS_3) Assisted Growth of $BaZrS_3$. To directly probe the role of BaS_3 in the low-temperature reaction mechanism for $BaZrS_3$, we first mix ground powders of BaS_3 and ZrS_2 followed by vacuum sealing in a glass ampule. Samples were annealed for 3 h at varying temperatures from 400 to 560 °C. When annealed at lower temperatures (400 and 450 °C), no phase change occurs and the precursor BaS_3 and ZrS_2 powders remain unchanged, as identified in the X-ray diffraction (XRD) data shown in Figure 1a. As the temperature is increased to 500 and 530 °C, several reactions are initiated as evidenced by the XRD (Figure 1a), summarized by (R1)−(R3). [Note that throughout the reactions we refer to $S_{(g.)}$, though gaseous sulfur exists as a polysulfide whose length depends on temperature; $S_{(g.)}$ is shown for clarity in quantifying the amount of sulfur released and required by each reaction.] First, the slow decomposition of BaS_3 into BaS_2 is observed.[27] Second, the complete conversion of ZrS_2 into ZrS_3 is found. As the formation of ZrS_3 requires more sulfur than is released from the partial decomposition of BaS_3, we also expect a slow reaction for the formation of $BaZrS_3$, though no $BaZrS_3$ phase can be easily identified in the XRD (either due the amount formed or poor crystallinity due to the low reaction temperature). The complete conversion of ZrS_2 into ZrS_3 suggests ZrS_3 participates in the slow formation of $BaZrS_3$ at these temperatures, discussed in more detail when directly using ZrS_3 as a precursor in Section 2.3.

$$BaS_3 \xrightarrow{Slow} BaS_2 + S_{(g.)} \quad (R1)$$

$$ZrS_2 + S_{(g.)} \xrightarrow{Fast} ZrS_3 \quad (R2)$$

$$BaS_3 + ZrS_3 \xrightarrow{Slow} BaZrS_3 + 3S_{(g.)} \quad (R3)$$

When the temperature is increased to 540 °C and higher, a dramatic change in the reaction occurs with virtually complete conversion of the precursors into $BaZrS_3$, with sharp, well-defined peaks in the XRD (Figure 1b). This change occurs close to the reported melting point of BaS_3 at 554 °C.[28] To better understand the reaction, BaS_3 was sealed individually in an ampule and annealed. During heating, yellow BaS_3 powder at room temperature gradually turned dark red and eventually into a black liquid droplet above 540 °C. This suggests the close relationship between the formation of the $BaZrS_3$ phase and liquid-phase BaS_3, described by (R4). Trace BaS_3 impurity peaks can also be found for all of the reactions at 540 °C and higher.

$$BaS_{3(liq.)} + ZrS_2 \xrightarrow{Fast} BaZrS_3 + 2S_{(g.)} \quad (R4)$$

To illustrate the fast reaction rate of the $BaS_{3(liq.)}$ growth mechanism in (R4), a series of reactions were performed at 550 °C (to ensure molten BaS_3) for various reaction times. XRD results for this time series are shown in Figure 1c, where phase formation and crystallinity of $BaZrS_3$ are virtually indistinguishable between the 5 min through 3 h reactions (see refined data in the SI).

The formation of $BaZrS_3$ was further confirmed by Raman spectroscopy, shown in Figure 1d for the same time series. This is primarily verified by the phonon modes for A_g^4 (134.4 cm^{-1}), (B_{2g}^4 + A_g^5) (156.6 cm^{-1}), A_g^6 (215.4 cm^{-1}), and B_{2g}^6 (221.2 cm^{-1}); note that shifts in the reference Raman data reported from Gross et al.[19] (measured at 14 K) are a result of the different measurement temperatures. Strong Raman scattering between 390 and 440 cm^{-1} is attributed to resonant forbidden LO-phonon scattering in $BaZrS_3$;[19] these features appear to broaden and weaken successively for the longer 1 and 3 h annealing times. In addition to $BaZrS_3$, the residual BaS_3 phase identified in XRD can also be seen in the Raman spectra (454.8 cm^{-1}). Furthermore, trace ZrS_3 (not observed in XRD) is identified by the small peak near 524 cm^{-1} for the short reaction times, as ZrS_3 reacts slower than ZrS_2 (see Section 2.3).

Here we propose a reactive, liquid-assisted growth mechanism for $BaZrS_3$ in $BaS_{3(liq.)}$ as a flux, as illustrated in Figure 2. Evidence for the liquid-assisted growth mechanism is primarily justified by the rapid crystallization of $BaZrS_3$ in as little as 5 min for temperatures coinciding with that greater than the melting point of BaS_3. The benefits of liquid-assisted growth can be realized through enhanced mass transport to and from grain boundaries and is typically associated with significant grain growth during short processing times at low temperatures (as reported here) relative to solid-state processes.[29] The existence of trace BaS_3 is not unexpected since this reactive flux is mixed in stoichiometric proportion. Thus, as the reaction nears completion the continuous distribution of this critical liquid phase disappears, leaving behind isolated pockets of BaS_3. For bulk powder reactions, it may be advantageous to use excess BaS_3 (see (R7)) to maintain a continuous liquid flux throughout the process, as BaS_3 can be readily removed from the final product (see Section 2.2). However, a thin-film geometry may mitigate this issue.

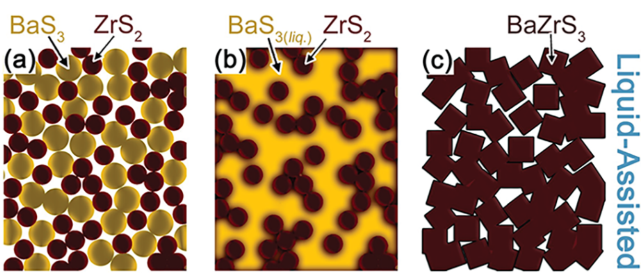

Figure 2. Schematic diagrams for three different stages in the liquid-assisted growth mechanism of $BaZrS_3$. (a) The initial mixture of BaS_3 and ZrS_2 powders at room temperature, (b) the initial formation of BaS_3 liquid at temperatures above ca. 540 °C, and (c) the recovered $BaZrS_3$ product.

To place our work in context with previously reported syntheses, annealing ZrS_2 and BaS is kinetically limited by mass transport during solid-state growth as no liquid flux is present (i.e., high temperatures and long reaction times are required). Alternatively, the inclusion of sulfur vapor during annealing (as in Wang et al.,[23] Comparotto et al.,[24] and Turnley et al.[22]) allows for the formation of BaS_3 from amorphous Ba or BaS precursors—resulting in a similar growth mechanism as identified here at low temperature. Interestingly, if the partial pressure of $S_{(g.)}$ is too high during annealing, the growth of ZrS_3 is increasingly favored relative to the formation of $BaZrS_3$. To avoid this, we propose the direct use of BaS_3 as a barium precursor rather than annealing in excess sulfur vapor; however, excess sulfur vapor released by (R4) is still important to stabilize this reaction, discussed below in Section 2.3. Freund et al.[30] recently attempted to fabricate a $BaZrS_3$ thin film by reacting BaS_3 (from sulfurization of sputtered BaS) with Zr metal; however, this was unsuccessful due to a low annealing temperature (≤460 °C) and the low reactivity of Zr metal as a precursor (see Section 2.3). Finally, the use of oxide precursors is thermodynamically limited, particularly the favorable formation of ZrO_2, if any oxygen is present during annealing (i.e., high temperatures and long reaction times are required). This thermodynamic limitation is removed in our work by using oxygen-free precursors.

2.2. Product Purification. To recover a pure $BaZrS_3$ product, the resulting powders for reactions at 540 °C and higher can be rinsed in H_2O, in which BaS_3 is highly soluble. Accordingly, the product from the 550 °C reaction (3 h) was rinsed 3 times via a dispersion in ultrapure H_2O, which was subsequently recovered with centrifugation. This was followed by a similar ethanol wash 2 times to remove any residual H_2O and vacuum drying at room temperature. During the first round of rinsing in H_2O, the initial blackish powder turned to a dark red precipitate following centrifugation (see inset of Figure 3b for the purified $BaZrS_3$ powder), while the supernatant turned yellow, indicating the dissolution of BaS_3. Fitted XRD of the recovered pure $BaZrS_3$ product is shown in Figure 3a (also see Figure S9). Rietveld refinement yields lattice parameters of a = 7.062 Å, b = 9.981 Å, and c = 7.0171 Å, which are in good agreement with reported values.[31] Similarly, the Raman spectrum of the purified powder in Figure 3b indicates the recovery of $BaZrS_3$.

Photoluminescence (PL), shown in Figure 3c, of the purified $BaZrS_3$ powder shows an emission peak near 698 nm (1.78 eV) which is in agreement with a range of previously reported values for $BaZrS_3$, shown by comparison in Figure S10. The PL emission is near the absorption edge measured via diffuse

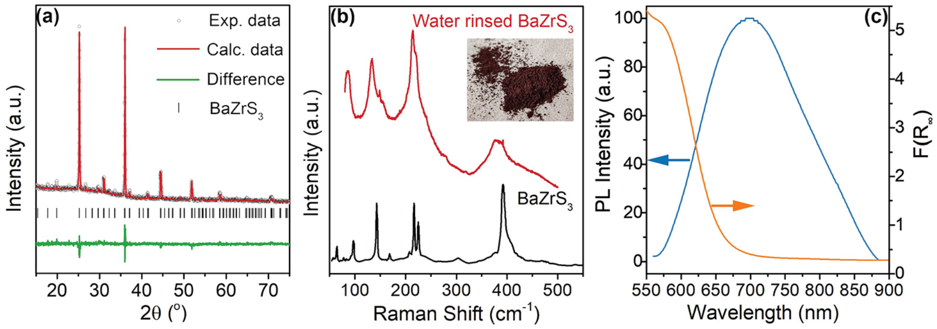

Figure 3. (a) XRD pattern with Rietveld refinement, (b) Raman spectrum, and (c) steady-state PL and absorption spectra for the water-washed $BaZrS_3$ product from the $BaS_3 + ZrS_2$ reaction at 550 °C for 3 h. Reference XRD shown in black labeled $BaZrS_3$ (PDF 01-073-0847). Reference Raman spectrum recorded at 14 K is from Gross et al.[19]

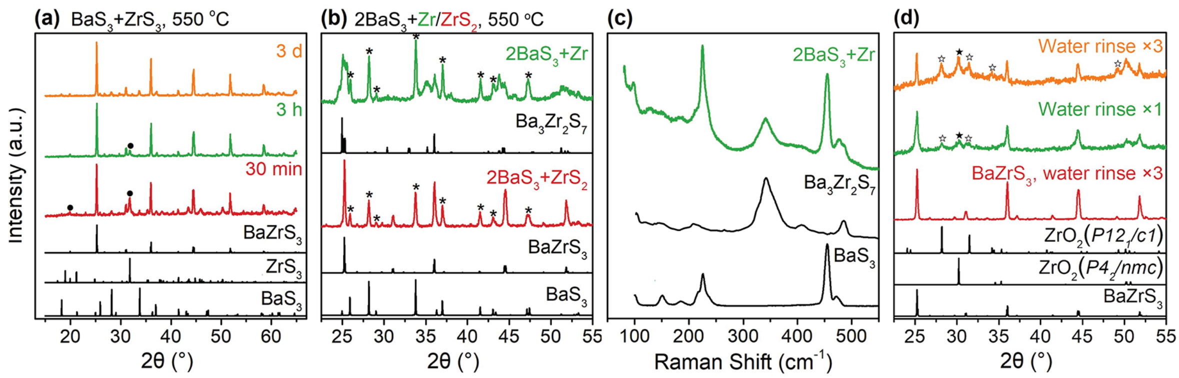

Figure 4. (a) XRD patterns of samples from reaction $BaS_3 + ZrS_3$ at 550 °C for various reaction times (circles label for ZrS_3). (b) XRD patterns of samples from BaS_3 + Zr-metal (green) and $BaS_3 + ZrS_2$ (red), both with excess BaS_3 (asterisks label for BaS_3) at 550 °C for 3 h. (c) Raman spectrum of the sample from BaS_3 + Zr-metal with excess BaS_3. $Ba_3Zr_2S_7$ reference is from Niu et al.[1] BaS_3 reference is measured Raman spectrum of BaS_3 precursor. (d) Powder XRD patterns of water-rinsed samples (orange and green for BaS_3 + Zr-metal and red for $BaS_3 + ZrS_2$) in (b) (filled stars label for ZrO_2 $P4_2/nmc$ and hollow stars label for ZrO_2 $P12_1/c1$). Reference XRD patterns are shown in black labeled by compound (BaS_3 PDF 01-073-1177, ZrS_3 PDF 01-080-0926, $BaZrS_3$ PDF 01-073-0847, ZrO_2 $P4_2/nmc$ PDF 01-079-1763, ZrO_2 $P12_1/c1$ PDF 01-072-1669).

reflectance (using the Kubelka−Munk transformation), also shown in Figure 3c. We refrain from extracting a band gap value from a Tauc plot of the transformed diffuse reflectance data based on the expected unusual nature of low energy transitions in the electronic structure of $BaZrS_3$.[4] We expect the optoelectronic properties to be strongly impacted by anionic defects, as similarly reported for A-site alkali earth metal and B-site Group IVB oxide perovskites.[32]

2.3. Zr Precursor Reactivity. It has been speculated that ZrS_3 can block the formation of $BaZrS_3$.[4] Therefore, variations in the Zr precursor were considered to understand the role of Zr in the reaction pathway. Accordingly, the $BaZrS_3$ synthesis reaction at 550 °C was repeated for various reaction times; however, ZrS_2 was replaced with ZrS_3. XRD data, shown in Figure 4a, illustrates that $BaZrS_3$ can also form under these reaction conditions. However, the decreasing presence of ZrS_3 is identified for reactions at both 30 min and 3 h. The virtually complete reaction of ZrS_3 can be observed if the reaction time is extended to 3 days. In all cases, trace BaS_3 is observed, as similarly seen when using ZrS_2 as a precursor. These results illustrate the reduced reactivity of ZrS_3 relative to ZrS_2 in the formation of $BaZrS_3$, reflected in (R3) and (R4). Accordingly, the use of excess sulfur conditions should be avoided to prevent ZrS_3 formation for the rapid growth of $BaZrS_3$ at low-temperature. However, ZrS_3 does not block the growth of $BaZrS_3$. It can be noted that both Ba in BaS_3 and Zr in ZrS_2 remain in a 12-fold and 6-fold coordination state, respectively, when transiting to $BaZrS_3$. In contrast, Zr is in an 8-fold coordination state in ZrS_3; the reduced coordination number of Zr in ZrS_2 may contribute to its increased reactivity.

The reactivity of Zr can be further reduced using elemental Zr-metal as a precursor. The stoichiometric reaction of $BaS_{3(liq.)}$ and Zr at 550 °C (3 h) results in the formation of the (relatively Zr-poor) Ruddlesden−Popper phase $Ba_3Zr_2S_7$ (Figure S11), described by (R5). This is better illustrated when BaS_3 is included in excess, described by (R6), with XRD results shown in Figure 4b (Figure S12). Raman spectroscopy, shown in Figure 4c, further verifies the formation of $Ba_3Zr_2S_7$ in excess BaS_3. However, when excess BaS_3 is reacted with ZrS_2 rather than Zr-metal, the $BaZrS_3$ phase is still recovered following (R7), with XRD also shown in Figure 4b. Therefore, the formation of the (relatively Zr-poor) $Ba_3Zr_2S_7$ is a result of the reduced Zr reactivity rather than barium excess.

$$4BaS_{3(liq.)} + 4Zr \rightarrow Ba_3Zr_2S_7 + BaS + 2ZrS_3 + S_{(g.)} \quad (R5)$$

$$3BaS_{3(liq.)} + 2Zr \xrightarrow{\text{Excess } BaS_3} Ba_3Zr_2S_7 + 2S_{(g.)} \quad (R6)$$

$$BaS_{3(liq.)} + ZrS_2 \xrightarrow{\text{Excess } BaS_3} BaZrS_3 + 2S_{(g.)} \quad (R7)$$

The appearance of BaS in (R5) is attributed to the relative reduction in excess sulfur vapor released by the reaction in comparison to (R4), (R6), and (R7). Low-temperature

https://doi.org/10.1021/acs.chemmater.3c00494
Chem. Mater. XXXX, XXX, XXX−XXX

annealing of BaS_3 in the absence of sulfur vapor results in the decomposition of BaS_3, as shown in Figure 1a (i.e., sulfur vapor stabilizes the BaS_3 phase). Therefore, a careful consideration of the sulfur vapor pressure is needed for the rapid reaction of pure-phase $BaZrS_3$ at low-temperature, even when elemental sulfur is not included as a precursor. For example, the reactor volume can make a significant contribution to the partial pressure of released $S_{(g.)}$.

An attempt was made to purify $Ba_3Zr_2S_7$ from the excess BaS_3 impurity with the H_2O rinse described in Section 2.2. However, we find $Ba_3Zr_2S_7$ is not stable in water. Figure 4d shows the XRD for the H_2O-rinsed $Ba_3Zr_2S_7$ product following 1× and 3× washing steps. In both cases, the $Ba_3Zr_2S_7$ phase has converted to $BaZrS_3$. Additionally, the formation of ZrO_2 ($P12_1/c1$ and $P4_2/nmc$) is observed. The ZrO_2 intensity increases with additional washing steps. Here we attribute the instability of the $Ba_3Zr_2S_7$ in water due to the intercalation of H_2O into the layered structure (Figure S13). The resulting exfoliated slabs retain a $BaZrS_3$ motif, with any resulting $Ba(OH)_2$ being soluble in the H_2O. The degradation of $BaZrS_3$ slabs into ZrO_2 may be a result of their small size, as they originate from an $n = 2$ Ruddlesden−Popper phase. We similarly find nanoscale $BaZrS_3$[20] is unstable to oxidation, which is also reported for $BaZrS_3$ with relatively reduced crystallinity.[4,33] In contrast, bulk crystalline $BaZrS_3$ is found to be H_2O-stable here and elsewhere.[18,33]

2.4. Vapor-Transport Growth of $BaZrS_3$ with Cl. The introduction of $BaCl_2$ into the solid-state syntheses of $BaZrS_3$ to lower the reaction temperature was first reported by Wang et al.[23] $BaZrS_3$ could be formed (in addition to BaS_3 and ZrO_2) at 450 °C over 7 days by reacting BaS with ZrS_2 in a specific excess of sulfur vapor, when 10% (molar) of the reactant BaS is replaced with $BaCl_2$. Little was reported regarding the mechanism of this low temperature synthesis. Similar results have been shown for (non-perovskite) $PbTiS_3$ and $BaTiS_3$.[34] We have previously shown (Section 2.1) that reaction temperatures lower than 540 °C cannot be used for the rapid reaction of BaS_3 with ZrS_2 into $BaZrS_3$. However, following Wang et al.,[23] if 10% (molar) BaS_3 is replaced with $BaCl_2$ we can achieve the formation of $BaZrS_3$ at 500 °C (3 h), with XRD of the resulting product shown in Figure 5.

In this chloride-containing reaction at 500 °C, liquid BaS_3 is no longer formed due to the low reaction temperature. However, the reaction rate is still relatively rapid as (primarily) $BaZrS_3$ forms in at least 3 h. Here we speculate a vapor-phase transport mechanism in the presence of chloride. Specifically, S_2Cl_2 can function as the vapor-phase transport agent, as described by (R8). S_2Cl_2 is commonly reported as a vapor-phase transport agent for the growth of single crystals, particularly for Group IVB transition metal chalcogenides.[35,36] Furthermore, S_2Cl_2 can form from the reversible reaction of metal chlorides in excess sulfur,[37,38] following (R9). S_2Cl_2 is a volatile (yellow) liquid at room temperature with a boiling point of 137 °C. Indeed, our work shows the reaction of $BaCl_2$ + $S_{(g.)}$ (500 °C, 3 h) forms a yellow liquid product when cooled to room temperature (though the instability of S_2Cl_2 in air makes further analysis challenging). Additionally, ZrS_2 can be readily dissolved in S_2Cl_2 to form a Zr-coordinated compound Zr-(S_2Cl_2). To demonstrate the S_2Cl_2 reaction mechanism, we also directly used S_2Cl_2 in the reaction rather than $BaCl_2$; XRD of the resulting product, Figure 5, shows similar results to the use of $BaCl_2$.

$$BaS_3 + ZrS_2 + 0.1S_2Cl_{2(g.)} \rightarrow BaZrS_3 + 2.2S_{(g.)} \quad (R8)$$

$$BaCl_2 + 3S_{(g.)} \rightarrow S_2Cl_{2(g.)} + BaS \quad (R9)$$

In the described chloride reactions, ZrS_3 forms as a secondary phase, following the now competitive reaction (R2), as sulfur is a product in the $BaZrS_3$ reaction (R8). However, a pure-phase $BaZrS_3$ product can be obtained (500 °C, 3 h) by reducing the amount of excess S following (R10); XRD for the product from this reaction is shown in Figure 5. The direct use of BaS_3 is not necessary at this reaction temperature since it occurs below the melting point of BaS_3, though is expected to form upon reaction with S. Note that in this reaction Zr metal was used, though no $Ba_3Zr_2S_7$ phase formed. This indicates a relatively balanced reactivity of BaS_3 and Zr-(S_2Cl_2) compared to Zr and ZrS_3 described in Section 2.3.

$$0.9BaS + 0.1BaCl_2 + 3S_{(g.)} + Zr \rightarrow BaZrS_3 + 0.1S_2Cl_2 + 0.7S \quad (R10)$$

These results indicate that $BaCl_2$ acts as a halide source for S_2Cl_2 formation. This is in contrast to speculation that $BaCl_2$ is beneficial to reduce the $S_{(g.)}$ pressure below that required for ZrS_3 formation, or that $BaCl_2$ acts as a precursor for BaS_3.[4,34] A proposed schematic for the vapor transport mechanism is depicted in Figure 6 in which accelerated mass transport of Zr via coordination with S_2Cl_2 allows for relatively rapid grain

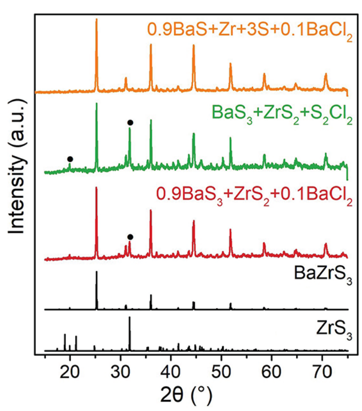

Figure 5. XRD patterns of reactions using Cl at 500 °C for 3 h (circles label ZrS_3). Reference XRD patterns are shown in black labeled by compound (ZrS_3 PDF 01-080-0926, $BaZrS_3$ PDF 01-073-0847.

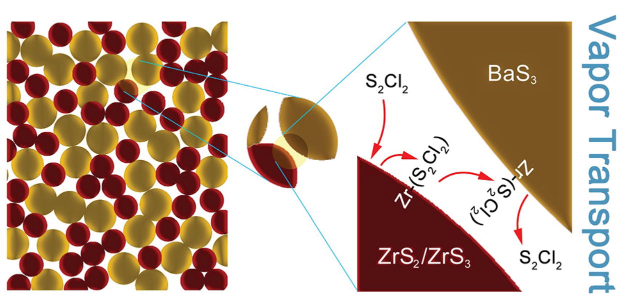

Figure 6. Schematic diagram of the vapor-transport growth mechanism. ZrS_2/ZrS_3 is shown in red and BaS_3 in yellow. A Zr-(S_2Cl_2) vapor-transport process is illustrated.

https://doi.org/10.1021/acs.chemmater.3c00494
Chem. Mater. XXXX, XXX, XXX−XXX

growth of $BaZrS_3$ (compared to the absence of S_2Cl_2 in which $BaZrS_3$ growth is limited for temperatures <540 °C).

2.5. Application of BaS_3-Flux for Additional ABS_3 Chalcogenides. Following the liquid-assisted growth mechanism described here-in (Section 2.1), $BaS_{3(liq.)}$ can similarly react with HfS_2, NbS_2, and TiS_2 at 550 °C (3 h) to readily form (chalcogenide perovskite) $BaHfS_3$, (hexagonal) $BaNbS_3$, and (hexagonal) $BaTiS_3$, respectively. XRD data are shown in Figure 7 following the water wash described in Section 2.2 (to

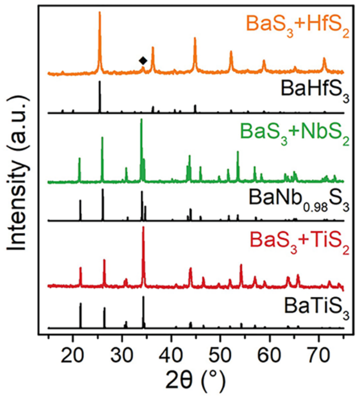

Figure 7. XRD patterns of samples from reaction of (BaS_3 + HfS_2), (BaS_3 + NbS_2), and (BaS_3 + TiS_2) at 550 °C for 3 h (diamond labels an unknown impurity peak in the $BaHfS_3$ product). Reference XRD patterns are shown in black labeled by compound ($BaTiS_3$ PDF 01-071-2000, $BaNb_{0.98}S_3$ PDF 01-083-0359, and $BaHfS_3$ from Lelieveld et al.[31]).

remove residual BaS_3). Diffuse reflectance data for $BaHfS_3$ (Figure S16) show a shift to higher energy compared to $BaZrS_3$, which is in agreement with its higher bandgap.[39] Images of the resulting powders as well as Rietveld refinement results can be found in the SI.

3. CONCLUSIONS

In this work, a low-temperature, liquid-assisted growth mechanism is demonstrated for Ba-based chalcogenide perovskites and related chalcogenides, including $BaZrS_3$, $Ba_3Zr_2S_7$, $BaHfS_3$, $BaNbS_3$, and $BaTiS_3$. The importance of liquid-BaS_3 is demonstrated for the rapid growth of these materials in as little as 5 min at temperature ≥540 °C. The reactivity of Zr is found to decrease from ZrS_2, Zr-(S_2Cl_2), to ZrS_3, ultimately resulting in the formation of the (relatively Zr-poor) Ruddlesden–Popper $Ba_3Zr_2S_7$ phase in the limit of elemental Zr-metal as a precursor. In this growth mechanism, we further demonstrate the role of $S_{(g.)}$ in the undesirable formation of ZrS_3 and in the stabilization of the desirable BaS_3 phase. The resulting $BaZrS_3$ from liquid-assisted grain growth can be purified from residual BaS_3-flux with a straightforward water wash. In contrast, $Ba_3Zr_2S_7$ is found to be unstable in water and converts to the $BaZrS_3$ phase, which oxidizes easily in water due to its small size. Lastly, in the absence of a liquid-phase, we also demonstrate a vapor-transport growth mechanism using S_2Cl_2 for the formation of $BaZrS_3$ at temperatures as low as 500 °C in at least 3 h.

$BaZrS_3$ is predicted to be thermodynamically stable relative to secondary binary phases, with the distorted perovskite phase as the ground state.[4] Our results support this conclusion. Although ZrS_3 forms in excess $S_{(g.)}$, it will react to form $BaZrS_3$ given enough time (kinetically limited). On the other hand, it has been proposed that $BaZrS_3$ may be unstable at $S_{(g.)}$ pressures where ZrS_3 forms;[4] we find that this is not the case for similar reasons. In contrast, at low $S_{(g.)}$ pressures, the reaction is kinetically limited by diffusion in the absence of liquid-BaS_3.

These results demonstrate the feasibility of scalable processing for the formation of chalcogenide perovskite thin-films at suitable temperatures, and several approaches to their formation and purification are shown.

4. EXPERIMENTAL METHODS

4.1. Materials. Sulfuric acid (H_2SO_4, 6.0 N, cat. No. 8330-16), barium chloride ($BaCl_2$, ≥97%, cat. No. B31-500), elemental sulfur (S, 99.50%, cat. No. AA1078536), titanium powder (Ti, 99.5% metals basis, cat. No. AA4310522), zirconium powder (Zr, cat. No. AA0041814), and hafnium powder (Hf, 99.6% metals basis excluding Zr, cat. No. AA1020106) were purchased from Fisher Scientific. Sulfur monochloride (S_2Cl_2, 98%, cat. No. 157759) was purchased from Sigma-Aldrich. Sulfur and zirconium powder were dried in a vacuum oven at 75 °C for 2 days before use. All other materials were used as received.

4.2. Precursor Synthesis. *BaS_3.* First, $Ba(OH)_2·8H_2O$ (32.546 g, 100 mmol) was dispersed in 200 mL of H_2O. The 6.0 N H_2SO_4 (33.3 mL, 100 mmol) was added slowly into the dispersion with vigorous agitation and an ice bath. The reaction was stopped at 5 h, and $BaSO_4$ was recovered by centrifugation. The product was washed with H_2O three more times before drying in the oven at 110 °C overnight. BaS was prepared by reduction of $BaSO_4$ with 4% hydrogen-balanced Ar in a tube furnace at 1000 °C for 12 h. The BaS product was a white powder. It was immediately taken into a N_2-filled glovebox and ground into fine white powder. BaS (5698 mg, 33.64 mmol) and elemental sulfur (2157 mg, 67.28 mmol) were mixed by grinding with an agate mortar and pestle in the glovebox. The mixture was then loaded into a dried borosilicate glass tube (OD 0.748 in, ID 0.606 in, length ca. 16 in) and flame-sealed under vacuum forming an ampule (length ca. 12 in). The ampule was heated in a muffle furnace from room temperature to 400 °C, with a ramp rate of 5 °C/min, and maintained for 12 h. The furnace was then turned off and allowed to slowly cool down to room temperature. The initial white BaS powder turned to lemon-yellow BaS_3 and was stored in the glovebox. Caution should be used when working with BaS_3 as barium polysulfides are water-soluble and known to be toxic upon ingestion, or can be an irritant upon skin exposure.

ZrS_2 and ZrS_3. Following the same mixing, evacuation, and sealing procedure of BaS_3 preparation, ZrS_3 was first made by reacting dried zirconium powder (Zr, 1095 mg, 12 mmol) and elemental sulfur (1154 mg, 36 mmol) in a dried borosilicate ampule (OD 0.748 in., ID 0.606 in., length ca. 12 in.). The mixture was heated in a muffle furnace to 300 °C, at 5 °C/min ramp rate, and maintained for 6 h. Next, it was heated in the same fashion to 400 °C, then 500 °C, at which point it was maintained 15 more hours. The furnace was then turned off and allowed to slowly cool down to room temperature. The initial dark gray mixture turned to a red powder of ZrS_3. For ZrS_2, the ZrS_3 powder was further decomposed in a tube furnace under ultrapure Ar. The tube furnace containing ZrS_3 was increased to 100 °C and maintained there for 30 min. The temperature was then increased to 800 °C within 1 h and maintained there for 2 h. The furnace was then turned off and allowed to slowly cool down to room temperature. The product ZrS_2 was a dark red powder and was stored in the glovebox.

HfS_2. Following the same mixing, evacuation, and sealing procedure of BaS_3 preparation, hafnium powder (1000 mg, 5.60 mmol) was mixed with elemental sulfur (359.2 mg, 11.20 mmol) into a dried quartz ampule (OD 0.55 in., ID 0.39 in., length ca. 13 in.). The mixture was heated in a muffle furnace to 750 °C from room temperature, at a 5 °C/min ramp rate, and maintained for 12 h. The furnace was then turned off and allowed to slowly cool down to room

https://doi.org/10.1021/acs.chemmater.3c00494
Chem. Mater. XXXX, XXX, XXX−XXX

temperature. A dark red/brown HfS_2 product formed and was stored in the glovebox.

TiS_2. Following the same mixing, evacuation, and sealing procedure of BaS_3 preparation, TiS_3 was first made by reacting Ti powder (1107 mg, 23.10 mmol) and elemental sulfur (2222 mg, 69.30 mmol) into a dried borosilicate ampule (OD 0.748 in., ID 0.606 in., length ca. 12 in.). Heating and cooling followed the procedure described for ZrS_3. The TiS_3 was then decomposed into TiS_2 in the same way as ZrS_2, though for 1.5 h instead of 2 h. The final product was greenish-yellow TiS_2 powder and was stored in the glovebox.

NbS_2. Following the same mixing, evacuation, and sealing procedure of BaS_3 preparation, niobium powder (591.6 mg, 6.37 mmol) was mixed with elemental sulfur (408.3 mg, 12.74 mmol) into a dried quartz ampule (OD 0.55 in., ID 0.39 in., length ca. 13 in.). The mixture was heated in a muffle furnace to 850 °C from room temperature, at 5 °C/min, and maintained for 12 h. The furnace was then turned off and allowed to slowly cool down to room temperature. A black NbS_2 product formed and was stored in the glovebox.

4.3. Ternary ABS_3 and $A_3B_2S_7$ Chalcogenides. In a typical reaction, 1.5 mmol fine powder of both A site source precursor (BaS or BaS_3) and B site source precursor (ZrS_2, ZrS_3, Zr-metal powder, HfS_2, NbS_2, TiS_2) were measured in the glovebox and ground together with an agate mortar and pestle. The mixture was subsequently transferred into a borosilicate glass tube (OD 0.5 in., ID 0.38 in., length ca. 6 in.) and flame-sealed under vacuum forming an ampule (ca. 3 in long). The ampule was transferred into a preheated muffle furnace at the desired temperature (560 °C, 550 °C, 540 °C, 530 °C, 500 °C, 450 °C, 400 °C) for different times (3 h, 1 h, 30 min, 5 min). The ampule was taken directly out of the furnace and cooled in air at the end of the reaction. For BaS_3 excess and chloride-involved reactions, the Zr precursor remained 1.5 mmol, and BaS_3 was adjusted accordingly. For the S_2Cl_2-involved reaction, S_2Cl_2 (12 μL) was first added to the end-sealed tube, followed by the addition of a stoichiometric mixture of BaS_3 and ZrS_2 on top. Extra caution should be used when working with corrosive S_2Cl_2. It is highly sensitive to water/moisture and hydrolyzes to release HCl mist and SO_2.

4.4. Ampule Sealing. Prior to sealing, all ampules were closed with a stopcock in the inert N_2 environment in the glovebox. Next, the closed tubes were taken out of the glovebox and directly attached to a roughing pump under vacuum for 10 min (S_2Cl_2 reactions were only pumped for 1 min). The ampules were then flame-sealed under vacuum (ca. 100−200 mTorr base pressure). Borosilicate tubes were sealed using a methylacetylene-propadiene propane (MAPP) torch while quartz tubes were sealed using an acetylene torch.

In the sulfurization reactions, sulfur quantities were as follows: (1) 38.0 mg/cm^3 for BaS into BaS_3, (2) 20.3 mg/cm^3 for Zr into ZrS_3, and (3) 19.5 mg/cm^3 for Ti into TiS_3, using borosilicate glass ampules with a 1.8 mm wall thickness. For the sulfurization reactions of (1) Hf into HfS_2 and (2) Nb into NbS_2, 14.1 mg/cm^3 and 16.0 mg/cm^3 of sulfur were used, respectively, with quartz glass ampules of 2.0 mm wall thickness. Although no elemental sulfur was used for ABX_3 syntheses, the sulfur generated in the reactions is estimated to be ca. 17.3 mg/cm^3 in borosilicate ampules with a 1.5 mm wall thickness by the end of the reactions. Under the conditions described, no ampule cracking was experienced. However, deviations from these values (e.g., increased sulfur amount, thinner wall thickness, or faster heating ramp rate) might increase the risk of pressure build-up and consequent ampule cracking.

4.5. Measurements. XRD measurments were performed with a PANalytical XPert Powder diffractometer using Cu Kα radiation at 45 kV and 40 mA and a zero-background holder. For the purified $BaZrS_3$, the XRD sample is a dropcast film. For all the other samples, powders were used for XRD measurements. Photoluminescence (PL), diffuse reflectance, and Raman measurements were performed on powder samples. PL was performed at 532 nm excitation. Diffuse reflectance measurements were performed with a white lamp and 99.9% diffuse reflectance standard. Both measurements utilized a NIREOS GEMINI interferometer and PicoQuant TimeHarp 260 time-correlated single photon counting system in "T2" mode to record interferograms, from which PL or reflectance spectra were reconstructed by fast Fourier transform. Raman spectroscopy for water rinsed $BaZrS_3$ and $2BaS_3$ + Zr-metal reaction was performed on a Horiba LabRAM ARAMIS with 785 nm wavelength excitation and a 10× objective. Raman spectra of the other samples were recorded using a Renishaw inVia Reflex Raman Microscope in a backscattering geometry with different excitation wavelengths including 785, 633, and 532 nm with a 50× objective. The measurement spot of each probed sample has been visually checked before and after measurement, indicating no laser damage. Furthermore, each laser has been calibrated by using a Si wafer.

ASSOCIATED CONTENT

Supporting Information

The Supporting Information is available free of charge at https://pubs.acs.org/doi/10.1021/acs.chemmater.3c00494.

Additional XRD of precursors, $BaZrS_3$, and $Ba_3Zr_2S_7$, Rietveld refinement for XRD presented here-in, comparison of PL data for $BaZrS_3$, intercalation schematic for $Ba_3Zr_2S_7$, and diffuse reflectance data for $BaHfS_3$ (PDF)

AUTHOR INFORMATION

Corresponding Author

Charles J. Hages − *Department of Chemical Engineering, University of Florida, Gainesville, Florida 32611, United States;* orcid.org/0000-0003-4054-1218; Email: c.hages@ufl.edu

Authors

Ruiquan Yang − *Department of Chemical Engineering, University of Florida, Gainesville, Florida 32611, United States*

Jessica Nelson − *Department of Chemical Engineering, University of Florida, Gainesville, Florida 32611, United States*

Calvin Fai − *Department of Chemical Engineering, University of Florida, Gainesville, Florida 32611, United States;* orcid.org/0000-0001-8866-3674

Hasan Arif Yetkin − *Department of Physics and Materials Science, University of Luxembourg, L-4422 Belvaux, Luxembourg*

Chase Werner − *Department of Chemical Engineering, University of Florida, Gainesville, Florida 32611, United States*

Merielle Tervil − *Department of Chemical Engineering, University of Florida, Gainesville, Florida 32611, United States*

Alexander D. Jess − *Department of Chemical Engineering, University of Florida, Gainesville, Florida 32611, United States*

Phillip J. Dale − *Department of Physics and Materials Science, University of Luxembourg, L-4422 Belvaux, Luxembourg*

Complete contact information is available at: https://pubs.acs.org/10.1021/acs.chemmater.3c00494

Notes

The authors declare no competing financial interest.

ACKNOWLEDGMENTS

C.J.H. acknowledges financial support from the SSMC program at the National Science Foundation (DMR-

2044859). H.A.Y. acknowledges financial support from University of Luxembourg.

■ REFERENCES

(1) Niu, S.; Milam-Guerrero, J.; Zhou, Y.; Ye, K.; Zhao, B.; Melot, B. C.; Ravichandran, J. Thermal stability study of transition metal perovskite sulfides. *J. Mater. Res.* **2018**, *33*, 4135−4143.

(2) Perera, S.; Hui, H.; Zhao, C.; Xue, H.; Sun, F.; Deng, C.; Gross, N.; Milleville, C.; Xu, X.; Watson, D. F.; Weinstein, B.; Sun, Y.-Y.; Zhang, S.; Zeng, H. Chalcogenide perovskites – an emerging class of ionic semiconductors. *Nano Energy* **2016**, *22*, 129−135.

(3) Swarnkar, A.; Mir, W. J.; Chakraborty, R.; Jagadeeswararao, M.; Sheikh, T.; Nag, A. Are Chalcogenide Perovskites an Emerging Class of Semiconductors for Optoelectronic Properties and Solar Cell? *Chem. Mater.* **2019**, *31*, 565−575.

(4) Sopiha, K. V.; Comparotto, C.; Márquez, J. A.; Scragg, J. J. S. Chalcogenide Perovskites: Tantalizing Prospects, Challenging Materials. *Advanced Optical Materials* **2022**, *10*, 2101704.

(5) Buffiere, M.; Dhawale, D. S.; El-Mellouhi, F. Chalcogenide Materials and Derivatives for Photovoltaic Applications. *Energy Technology* **2019**, *7*, 1900819.

(6) Jaramillo, R.; Ravichandran, J. In praise and in search of highly-polarizable semiconductors: Technological promise and discovery strategies. *APL Materials* **2019**, *7*, 100902.

(7) Nishigaki, Y.; Nagai, T.; Nishiwaki, M.; Aizawa, T.; Kozawa, M.; Hanzawa, K.; Kato, Y.; Sai, H.; Hiramatsu, H.; Hosono, H.; Fujiwara, H. Extraordinary Strong Band-Edge Absorption in Distorted Chalcogenide Perovskites. *Solar RRL* **2020**, *4*, 1900555.

(8) Wu, X.; Gao, W.; Chai, J.; Ming, C.; Chen, M.; Zeng, H.; Zhang, P.; Zhang, S.; Sun, Y. Y. Defect tolerance in chalcogenide perovskite photovoltaic material $BaZrS_3$. *Science China Materials* **2021**, *64*, 2976−2986.

(9) Meng, W.; Saparov, B.; Hong, F.; Wang, J.; Mitzi, D. B.; Yan, Y. Alloying and Defect Control within Chalcogenide Perovskites for Optimized Photovoltaic Application. *Chem. Mater.* **2016**, *28*, 821−829.

(10) Hahn, H.; Mutschke, U. Untersuchungen über ternäre Chalkogenide. XI. Versuche zur Darstellung von Thioperowskiten. *Zeitschrift fur anorganische und allgemeine Chemie* **1957**, *288*, 269−278.

(11) Clearfield, A. The synthesis and crystal structures of some alkaline earth titanium and zirconium sulfides. *Acta Crystallogr.* **1963**, *16*, 135−142.

(12) Márquez, J. A.; Rusu, M.; Hempel, H.; Ahmet, I. Y.; Kölbach, M.; Simsek, I.; Choubrac, L.; Gurieva, G.; Gunder, R.; Schorr, S.; Unold, T. $BaZrS_3$ Chalcogenide Perovskite Thin Films by H_2S Sulfurization of Oxide Precursors. *J. Phys. Chem. Lett.* **2021**, *12*, 2148−2153.

(13) Wei, X.; et al. Realization of $BaZrS_3$ chalcogenide perovskite thin films for optoelectronics. *Nano Energy* **2020**, *68*, 104317.

(14) Yu, Z.; Wei, X.; Zheng, Y.; Hui, H.; Bian, M.; Dhole, S.; Seo, J. H.; Sun, Y. Y.; Jia, Q.; Zhang, S.; Yang, S.; Zeng, H. Chalcogenide perovskite $BaZrS_3$ thin-film electronic and optoelectronic devices by low temperature processing. *Nano Energy* **2021**, *85*, 105959.

(15) Surendran, M.; Chen, H.; Zhao, B.; Thind, A. S.; Singh, S.; Orvis, T.; Zhao, H.; Han, J.-K.; Htoon, H.; Kawasaki, M.; Mishra, R.; Ravichandran, J. Epitaxial thin films of a chalcogenide perovskite. *Chem. Mater.* **2021**, *33*, 7457−7464.

(16) Comparotto, C.; Davydova, A.; Ericson, T.; Riekehr, L.; Moro, M. V.; Kubart, T.; Scragg, J. Chalcogenide Perovskite $BaZrS_3$: Thin Film Growth by Sputtering and Rapid Thermal Processing. *ACS Applied Energy Materials* **2020**, *3*, 2762−2770.

(17) Sadeghi, I.; Ye, K.; Xu, M.; Li, Y.; LeBeau, J. M.; Jaramillo, R. Making $BaZrS_3$ Chalcogenide Perovskite Thin Films by Molecular Beam Epitaxy. *Adv. Funct. Mater.* **2021**, *31*, 2105563.

(18) Gupta, T.; et al. An Environmentally Stable and Lead-Free Chalcogenide Perovskite. *Adv. Funct. Mater.* **2020**, *30*, 2001387.

(19) Gross, N.; Sun, Y.-Y.; Perera, S.; Hui, H.; Wei, X.; Zhang, S.; Zeng, H.; Weinstein, B. Stability and band-gap tuning of the chalcogenide perovskite $BaZrS_3$ in Raman and optical investigations at high pressures. *Physical Review Applied* **2017**, *8*, 044014.

(20) Yang, R.; Jess, A. D.; Fai, C.; Hages, C. J. Low-Temperature, Solution-Based Synthesis of Luminescent Chalcogenide Perovskite $BaZrS_3$ Nanoparticles. *J. Am. Chem. Soc.* **2022**, *144*, 15928−15931.

(21) Zilevu, D.; Parks, O. O.; Creutz, S. E. Solution-phase synthesis of the chalcogenide perovskite barium zirconium sulfide as colloidal nanomaterials. *Chem. Commun.* **2022**, *58*, 10512−10515.

(22) Turnley, J. W.; Vincent, K. C.; Pradhan, A. A.; Panicker, I.; Swope, R.; Uible, M. C.; Bart, S. C.; Agrawal, R. Solution Deposition for Chalcogenide Perovskites: A Low-Temperature Route to $BaMS_3$ Materials (M = Ti, Zr, Hf). *J. Am. Chem. Soc.* **2022**, *144*, 18234−18239.

(23) Wang, Y.; Sato, N.; Yamada, K.; Fujino, T. Synthesis of $BaZrS_3$ in the presence of excess sulfur. *J. Alloys Compd.* **2000**, *311*, 214−223.

(24) Comparotto, C.; Ström, P.; Donzel-Gargand, O.; Kubart, T.; Scragg, J. J. Synthesis of $BaZrS_3$ Perovskite Thin Films at a Moderate Temperature on Conductive Substrates. *ACS Applied Energy Materials* **2022**, *5*, 6335−6343.

(25) Niu, S.; Huyan, H.; Liu, Y.; Yeung, M.; Ye, K.; Blankemeier, L.; Orvis, T.; Sarkar, D.; Singh, D. J.; Kapadia, R.; Ravichandran, J. Bandgap Control via Structural and Chemical Tuning of Transition Metal Perovskite Chalcogenides. *Adv. Mater.* **2017**, *29*, 1604733.

(26) Vincent, K. C.; Agarwal, S.; Turnley, J. W.; Agrawal, R. Liquid Flux−Assisted Mechanism for Modest Temperature Synthesis of Large-Grain BaZrS3 and BaHfS3 Chalcogenide Perovskites. *Advanced Energy and Sustainability Research* **2023**, *4*, 2300010.

(27) v. Schnering, H. G.; Goh, N. K. Die Strukturen der Polysulfide BaS_3, SrS_3, BaS_2 und SrS_2. *Die Naturwissenschaften* **1974**, *61*, 272.

(28) Lide, D. R., Ed. *CRC Handbook of Chemistry and Physics*, 73rd ed.; CRC Press: 1992; pp 4−43.

(29) Hages, C. J.; Koeper, M. J.; Miskin, C. K.; Brew, K. W.; Agrawal, R. Controlled Grain Growth for High Performance Nanoparticle-Based Kesterite Solar Cells. *Chem. Mater.* **2016**, *28*, 7703−7714.

(30) Freund, T.; Cicconi, M. R.; Wellmann, P. J. Fabrication of Bariumtrisulphide Thin Films as Precursors for Chalcogenide Perovskites. *Physica Status Solidi B* **2022**, *259*, 2200094.

(31) Lelieveld, R.; IJdo, D. J. W. Sulphides with the GdFeO3 structure. *Acta Crystallographica Section B Structural Crystallography and Crystal Chemistry* **1980**, *36*, 2223−2226.

(32) Tufte, O. N.; Chapman, P. W. Electron Mobility in Semiconducting Strontium Titanate. *Phys. Rev.* **1967**, *155*, 796−802.

(33) Wang, Y.; Sato, N.; Fujino, T. Synthesis of $BaZrS_3$ by short time reaction at lower temperatures. *J. Alloys Compd.* **2001**, *327*, 104−112.

(34) Wang, Y.; Sato, N.; Yamada, K.; Fujino, T. Effect of Halide Addition on the Syntheses of $PbTiS_3$ and Ba_xTiS_y in Sulfur Melt. *Shigen-to-Sozai* **2000**, *116*, 703−710.

(35) Lévy, F.; Berger, H. Single crystals of transition metal trichalcogenides. *J. Cryst. Growth* **1983**, *61*, 61−68.

(36) Binnewies, M.; Glaum, R.; Schmidt, M.; Schmidt, P. *Chemical Vapor Transport Reactions*; De Gruyter: 2012; Chapter 7, pp 321−402.

(37) Kleinert, P.; Funke, A. Über Reaktionen von Magnesiumferrit und Magnetit mit Dischwefeldichlorid. *Die Naturwissenschaften* **1960**, *47*, 106−107.

(38) Engelke, F.; Zare, R. Crossed-beam chemiluminescence: The alkaline earth rearrangement reaction $M + S_2Cl_2 \rightarrow S_2^* + MCl_2$. *Chem. Phys.* **1977**, *19*, 327−340.

(39) Sun, Y.; Agiorgousis, M. L.; Zhang, P.; Zhang, S. Chalcogenide perovskites for photovoltaics. *Nano Lett.* **2015**, *15*, 581−585.